

# Morphology of atherosclerotic coronary arteries

Margaret N. Holme<sup>a,b,c</sup>, Georg Schulz<sup>a</sup>, Hans Deyhle<sup>a</sup>, Simone Elke Hieber<sup>a</sup>, Timm Weitkamp<sup>d</sup>, Felix Beckmann<sup>e</sup>, Julia Herzen<sup>e</sup>, Johannes A. Lobl<sup>f</sup>, Fabrizio Montecucco<sup>c</sup>, François Mach<sup>c</sup>, Andreas Zumbuehl<sup>b</sup>, Till Saxer<sup>c</sup>, and Bert Müller<sup>\*a</sup>

<sup>a</sup>Biomaterials Science Center, University of Basel, c/o University Hospital, 4031 Basel, Switzerland;

<sup>b</sup>Department of Chemistry, University of Fribourg, 1700 Fribourg, Switzerland;

<sup>c</sup>Cardiology Division, University Hospitals of Geneva, 1211 Geneva, Switzerland;

<sup>d</sup>Synchrotron Soleil, 91190 Gif-sur-Yvette, France;

<sup>e</sup>Institute of Materials Research, Helmholtz-Zentrum Geesthacht, 21502 Geesthacht, Germany;

<sup>f</sup>Department of Clinical Pathology, University Hospitals of Geneva, 1211 Geneva, Switzerland

## ABSTRACT

Atherosclerosis, the narrowing of vessel diameter and build-up of plaques in coronary arteries, leads to an increase in the shear stresses present, which can be used as a physics-based trigger for targeted drug delivery. In order to develop appropriate nanometer-size containers, one has to know the morphology of the critical stenoses with isotropic micrometer resolution. Micro computed tomography in absorption and phase contrast mode provides the necessary spatial resolution and contrast. The present communication describes the pros and cons of the advanced laboratory and synchrotron radiation-based approaches in the visualization of diseased human and murine arteries. Using registered datasets, it also demonstrates that multi-modal imaging, including established histology, is even more powerful. The tomography data were evaluated with respect to cross-section, vessel radius and maximal constriction. The average cross-section of the diseased human artery ( $2.31 \text{ mm}^2$ ) was almost an order of magnitude larger than the murine one ( $0.27 \text{ mm}^2$ ), whereas the minimal radius differs only by a factor of two ( $0.51 \text{ mm}$  versus  $0.24 \text{ mm}$ ). The maximal constriction, however, was much larger for the human specimen (85% versus 49%). We could also show that a plastic model used for recent experiments in targeted drug delivery represents a very similar morphology, which is, for example, characterized by a maximal constriction of 82%. The tomography data build a sound basis for flow simulations, which allows for conclusions on shear stress distributions in stenosed blood vessels.

**Keywords:** Atherosclerosis: vessel morphology, shear stress, human coronary artery, mouse model, plaque, micro computed tomography, phase tomography, histology

## 1. INTRODUCTION

Cardiovascular disease is the number one cause of morbidity and mortality in modern society. In 2008 it was responsible for 30% of all deaths globally [1]. The disease is characterized by the natural progression of lesion formation followed by lipid core expansion, macrophage accumulation and finally formation of a fibrose cap [2]. In the latter stages, the arteries become increasingly rigid and significantly stenosed due to the space occupied by the diseased tissue. In the acute case of plaque rupture, i.e. myocardial infarction (MI), the vasodilator nitroglycerine is often administered to open up and widen the stenosed arteries to allow for the reperfusion of blood before ischemic events. Unfortunately, owing to the systemic effect of such vasodilators, their administration has to be carefully monitored or withdrawn prematurely to minimize the unavoidable side effects such as systemic hypotension.

It is well known that the constriction in critically stenosed arteries leads to local endogenous shear stresses that are significantly higher than those found in the healthy vascular system [3]. Encapsulating the vasodilators (nitroglycerine) in shear-sensitive nanocontainers, e.g. liposomes [4], could alleviate these problems. Targeting shear stresses such as those found in, for example, an 80%-stenosed artery would ensure the drug is delivered to the diseased artery but significantly less to the surrounding healthy vascular system. In order to better understand the local shear stress changes using flow simulations, the morphology of critically stenosed arteries must be uncovered down to the micrometer level.

\*bert.mueller@unibas.ch; phone +41 61 265 9659; fax +41 61 265 9699; www.bmc.unibas.ch

The imaging of plaque-containing arteries is challenging, as the simultaneous artifact-free visualization of hard and soft tissue components needs precise knowledge on the preparation including embedding and on the choice of imaging modalities and parameters. Nevertheless, micro computed tomography ( $\mu$ CT) is one of the most powerful techniques that enable the experimentalist to nondestructively image microstructures with isotropic resolution in the three-dimensional (3D) space. The presence of the plaque within the blood vessels means that higher photon energies are required to avoid streak artifacts. This choice, however, leads to a decrease in the density resolution of the soft tissue components since higher energy X rays exhibit much less interaction probability in the conventional absorption contrast. In synchrotron-radiation based  $\mu$ CT in phase contrast mode (phase tomography) using hard X rays this dependence is much weaker [5]. Therefore, phase tomography might be much better suited to visualize the plaque-containing stenosed arteries.

Here, we report data on human and mouse arteries acquired using  $\mu$ CT. Micro computed tomography using a conventional or advanced laboratory setup (laboratory  $\mu$ CT) provides a user-friendly imaging modality that can be rather easily implemented in a research lab, and is suitable for segmenting the lumen morphology and understanding the extent of stenosis in a given vessel. It is also well suited to investigate plastic models of the human vascular system such as those recently applied to demonstrate the efficacy of nanocontainers in targeted drug delivery [4]. One can quantify the degree of occlusion in a polymethylmethacrylate (PMMA) model of the diseased situation with respect to the healthy morphology. Subsequently the model data can be quantitatively compared with the actual morphology of stenosed human or animal arteries. In search of an animal model for further testing of targeted drug delivery and following the advice of international experts, we measured two mouse abdominal aortas using phase SR $\mu$ CT. One has to recognize that mice have an intrinsically higher shear stress due to their smaller vessel sizes. It is, however, rather simple to breed plaque in their arteries. Tomography data can be the basis of flow simulations to determine how far experiments with small animals resemble the situation of patients.

Phase tomography [6, 7] provides significantly better contrast in soft tissues than both advanced laboratory  $\mu$ CT and SR $\mu$ CT in absorption contrast mode. Therefore, this approach allows the differentiation between several tissue types similar to well-established histology. We know, however, that the combination of imaging techniques, often termed multi-modal imaging, is even more powerful. In this communication on human coronary arteries we show registered slices of multi-modal imaging.

## 2. MATERIALS AND METHODS

### 2.1 PMMA model

Previous *in vitro* studies to evaluate the shear stress sensitivity of nanometer-size vesicles were based on a flow system akin to the human vascular system [4]. The aim of this previous study was to identify lipid formulations that react to endogenous shear stresses in stenosed human coronary arteries as a physical release trigger. For this reason, a PMMA model (Elastrat, Lausanne, Switzerland) of a healthy and diseased artery was built and incorporated into the experimental setup. To assess the morphology of this model and to quantitatively compare it with human vessel morphology, it was visualized using an advanced laboratory  $\mu$ CT by means of a nanotom m (Phoenix|x-ray, GE Sensing & Inspection Technologies GmbH, Wunstorf, Germany) using a 180 kVp / 15 W nanofocus X-ray source. The model was measured with an accelerating voltage of 120 kVp, a beam current of 100  $\mu$ A, and 2 s exposure time, with a 0.2 mm aluminum filter to increase the mean photon energy. 1000 equiangular projections were recorded over 360° in a field of view of 1300  $\times$  2400 pixels, pixel size 25  $\mu$ m. Reconstruction of the projections was carried out using a cone beam filtered back-projection algorithm of phoenix datos|x 2.0.1 - RTM (GE Sensing & Inspection Technologies GmbH, Wunstorf, Germany). The reconstructed 3D dataset contains 16-bit values, which correlate to the local X-ray absorption in the specimen.

### 2.2 Mouse aortas

Apolipoprotein E deficient mice (ApoE<sup>-/-</sup>) in a C57BL/6J background were obtained from the Charles River Laboratories. At eleven weeks of age, two males were fed with a high-cholesterol diet (HCD; 1.25% cholesterol) for an additional eleven weeks. Then, the animals were euthanized and perfused for five minutes with phosphate buffer saline before the abdominal aortas were collected [8]. These tissues were immediately immersed in 4% paraformaldehyde (PFA) fixative for 24 h before analysis. This protocol was approved by the local ethical committee and Swiss authorities as well as conformed to the 'position of the American Heart Association on Research Animal Use'.

The phase tomography measurements were carried out using a Talbot-Lau interferometer at the beamline W 2 (HASYLAB at DESY, Hamburg, Germany), operated by the HZG Research Center [6, 9]. The grating interferometer consisted of three gratings: the source grating (period 22.9  $\mu\text{m}$ ; gold height 130  $\mu\text{m}$ ), the phase grating (period 4.33  $\mu\text{m}$ ; silicon height about 60  $\mu\text{m}$ ) and the analyzer grating (period 2.4  $\mu\text{m}$ ; gold height: 150  $\mu\text{m}$ ). Source and phase gratings were fabricated at the Paul Scherrer Institut (Villigen, Switzerland). The analyzer gold grating was produced at the Karlsruhe Institute of Technology (Karlsruhe, Germany). The photon energy was set to 31 keV corresponding to the third fractional Talbot order. The X-ray detector consisted of a  $\sim 580$   $\mu\text{m}$ -thick  $\text{CdWO}_4$  scintillator lens-coupled to a CCD camera. The PL09000 CCD camera (Finger Lakes Instrumentations, New York, USA) had an active area of  $3056 \times 3056$  pixels, pixel size 12  $\mu\text{m}$ . For each projection a phase-stepping scan was performed, in which a set of images at eight different positions of the phase grating over two periods was recorded. The moderate optical magnification of 5.41 gave rise to an effective pixel size of 2.22  $\mu\text{m}$  with a field of view of  $6.77 \times 6.77$   $\text{mm}^2$ . The spatial resolution determined from a highly absorbing edge in absorption mode was 5.18  $\mu\text{m}$  [10]. Tomographic reconstruction was performed using a modified filter kernel in combination with standard filtered back-projection algorithm [6, 11].

### 2.3 Multi-modal imaging of atherosclerotic human coronary arteries

Two 2.5 cm-long sections from different human coronary arteries were explanted *post mortem* at the Institute of Forensic Medicine, University Medical Center, Hamburg-Eppendorf. They were subsequently immersed in 4% PFA fixative for more than 10 h, then dehydrated by soaking under reduced pressure overnight in alcohol followed by xylene after which it was immersed in molten paraffin (60  $^\circ\text{C}$ ) and cooled to room temperature. After SR $\mu$ CT-measurements (not reported here), the paraffin was removed by heating the artery to 60  $^\circ\text{C}$  then washing in a Histokinette (Tissue-TEK VIP E3000) for 12 h under reduced pressure in xylene, alcohol then water. The artery was immersed in decalcifier (distilled water : formic acid : PFA, 87 : 8 : 5 v/v) at a temperature of 37  $^\circ\text{C}$  for two days. After complete decalcification, a 2 mL sample of decalcifier in which the artery is immersed does not become milky if mixed with 1 mL ammonium oxalate (5%) and 1 mL ammonia (5%). The artery was then dehydrated and immersed in molten paraffin as described above. Once the paraffin had cooled, the block was trimmed to the part containing the artery and smoothed by rubbing to avoid air bubbles on the surface during measurement.

**Advanced laboratory  $\mu$ CT:** The morphology of a human coronary artery was assessed first by laboratory  $\mu$ CT using a nanotom m (Phoenix|x-ray, GE Sensing & Inspection Technologies GmbH, Wunstorf, Germany) and 180 kVp / 15 W nanofocus X-ray source, analogously to the PMMA model described above. An accelerating voltage of 60 kVp, a beam current of 310  $\mu\text{A}$ , and 1.2 s exposure time were used together with a 0.5 mm-thick aluminum filter to increase the mean photon energy. 1000 equiangular projections were measured over 360 $^\circ$ . The field of view was  $1300 \times 2400$  pixels, pixel size 17.78  $\mu\text{m}$ . Reconstruction of the projections was carried out using a cone beam filtered back-projection algorithm of the software phoenix datos|x 2.0.1 - RTM (GE Sensing & Inspection Technologies GmbH, Wunstorf, Germany) with a ring artifact removal routine.

**Absorption SR $\mu$ CT:** The absorption contrast-based SR $\mu$ CT measurement was carried out at the beamline BW 2 (HASYLAB, DESY, Germany) operated by the Helmholtz-Zentrum Geesthacht [12]. The highly intense, collimated X-ray beam was monochromatized by means of a fixed-exit double crystal monochromator (Si(111)-crystals) to realize a photon energy of 14 keV with a bandwidth of 0.01%. The tomography set-up was installed 40 m from the radiation source and consisted of the sample manipulator and two-dimensional detection unit. The sample manipulator was used for both precise sample rotation and sample translation, so the photon distribution within the X-ray beam could be recorded without specimen for normalization. The X-ray detection unit was a luminescent screen (500- $\mu\text{m}$ -thick  $\text{CdWO}_4$  single crystal), optical lens (Nikkor 35 mm focal length, Nikon Inc., Tokyo, Japan), and charge-coupled device (CCD) camera (KX2, Apogee Instruments Inc., Roseville, CA, USA, 14-bit digitization at 1.25 MHz,  $1536 \times 1024$  pixels, pixel size 9  $\mu\text{m}$ ). The incident X rays were converted into visible light by the luminescent screen, projected with the magnification of 3.05 onto the CCD chip [13] resulting in an effective pixel size of 2.95  $\mu\text{m}$ . To increase photon statistics, and therefore the contrast in the reconstructed slices, projections were binned by a factor of two [14]. The spatial resolution determined from a highly absorbing edge was 5.28  $\mu\text{m}$  [11].

**Phase tomography:** The phase tomography measurement was carried out at the beamline ID 19 (ESRF, Grenoble, France). Artifacts were expected by the strong phase shift at the surface of the artery-containing paraffin block with surrounding air, caused by the prominent difference in decrement of the refractive indexes. To minimize related artifacts, the specimen was immersed in a water bath with parallel PMMA plates arranged perpendicular to the incoming X-ray beam. To ensure that no air bubbles formed on the specimen's surface, it was smoothed by rubbing gently before immersion in the bath. A photon energy of 23 keV was selected using a double-crystal Si(111) monochromator in Bragg

geometry. The specimen was situated 10 cm upstream from the beam-splitter grating (4.785  $\mu\text{m}$  periodicity, 29  $\mu\text{m}$  Si structure height). With a distance between source and interferometer of 150 m and a distance between the gratings of 481 mm (ninth Talbot order), the ratio of the grating periods was matched to the beam divergence [15]. The detector, placed about 3 cm downstream of the analyzer grating with a periodicity of 2.400  $\mu\text{m}$  and a structure height of 50  $\mu\text{m}$ , was a lens-coupled scintillator and CCD system using a FReLoN 2K (Fast-Readout, Low-Noise, ESRF Grenoble, France) CCD with 2048  $\times$  2048 pixels. The effective pixel size corresponded to 5.4  $\mu\text{m}$ . The field of view was 10.4  $\times$  11.0  $\text{mm}^2$ . Projection radiographs were taken at an angular step size of 0.36 $^\circ$  (999 intervals over 360 $^\circ$  scan range), with 1.2 s exposure time. At each projection angle, four phase-stepping images were taken over one period of the interferometer fringe pattern. The reader is referred to the literature for detailed descriptions of grating interferometry and of the phase-stepping method [7] and for the details of the instrument used in this study [16]. The phase-contrast projection dataset was reconstructed using a modified filter kernel (Hilbert transform) in combination with a standard filtered back-projection algorithm [17-19].

**Histology:** The paraffin embedded artery was prepared into 2 to 4  $\mu\text{m}$ -thin lateral sections. Maintaining the artery in the same paraffin embedding ensured the unchanged morphology between  $\mu\text{CT}$ -measurements and histological preparation. Since it is time consuming to prepare each slice, the preparation of all sequential slices is impossible within a reasonable time frame. Therefore, every 20<sup>th</sup> slice from the paraffin ribbon was mounted on a glass slide and stained with Hematoxylin and Eosin (H&E) stain. Each slice was photographed using a Nikon Eclipse 80i microscope and camera at 10 $\times$  magnification in an average of 20 sections, which were stitched together using the stitching plug-in [20] available in Fiji software (ImageJ version 1.45k, EMBL, Germany) [21] to give color images of on average 4500  $\times$  5500 pixels, pixel size 0.5  $\mu\text{m}$ .

### 3. RESULTS

#### 3.1 PMMA model artery

In the center of Figure 1 the model with the two channels that represent a healthy vessel and an atherosclerotic human coronary artery are displayed. One easily recognizes the morphology of the diseased vessel on the left and the morphology of the healthy vessel on the right. The lumen is easily extracted by means of thresholding [22]. The cross-sectional area of the lumen for each vessel in the individual slices is determined using computer code (MATLAB R2010b). The right diagram in Figure 1 with the graph in red color shows the variation of the cross-section as a function of position (height). The value varies by a maximum of 7% between 6.04 and 6.49  $\text{mm}^2$ . The diagram on the left in Figure 1 with the blue-colored graph corresponds to the diseased vessel and the cross-sectional area fluctuates between 1.17 and 6.43  $\text{mm}^2$ , which is more than a factor of five. This means that the maximal cross section in both cases is identical within the error bars, whereas the minimal cross sections differ by more than a factor of five.

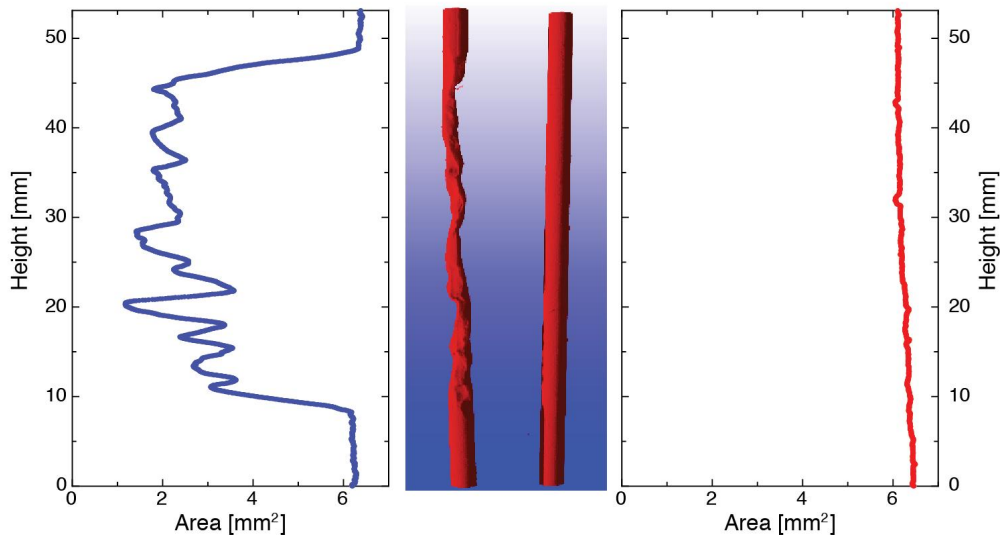


Figure 1. Cross-sectional area of the inner volume of a diseased (left) and healthy (right) artery model derived from laboratory  $\mu\text{CT}$  measurements. In the center, the data are represented as 3D rendering.

### 3.2 Mouse aortas

The mouse abdominal aortas were investigated using synchrotron radiation-based phase tomography to determine their morphology on the micrometer scale. The vessel walls exhibited a larger real part of the refractive index in comparison with the surrounding tissues and PFA solution in the Eppendorf container. Thus, it was rather simple to segment the lumen (see Figure 2) using the region-growing tool in VG Studio Max 2.1 (Volume Graphics, Heidelberg, Germany). The associated 3D renderings in Figure 2 were generated in VG Studio Max 2.1 by means of thresholding [22] and rendered using the settings Volume Renderer (Scatter HQ) (Figure 2, top, bisected artery) and Scatter HQ (v1.2) (Figure 2, bottom left).

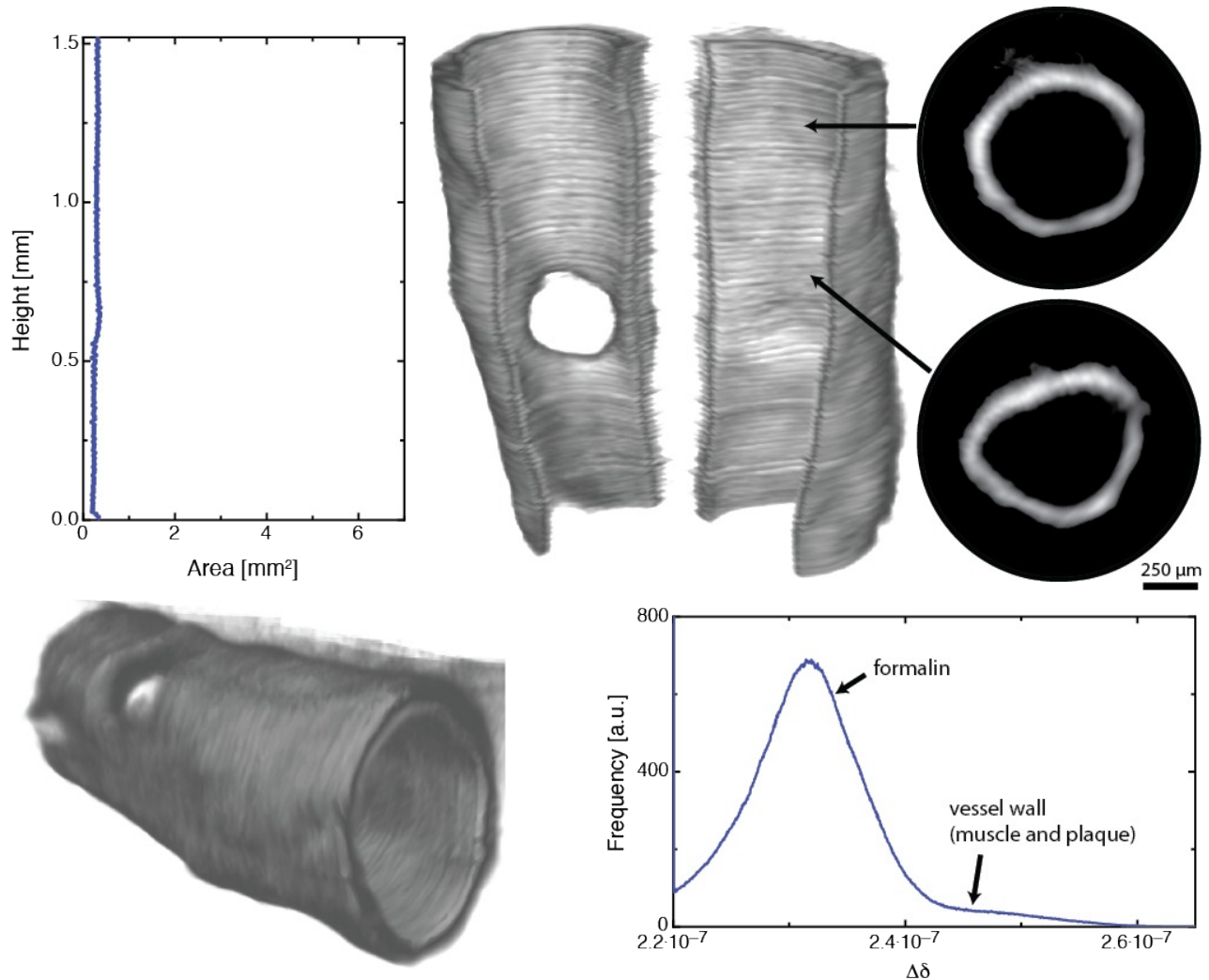


Figure 2: Morphology of a stenosed mouse aorta from a phase SR $\mu$ CT measurement. Top, left to right: diagram of the cross sectional area of the lumen with axes comparable to the diagrams in Figure 1, 3D rendering of the artery bisected and opened up down the middle, with two selected cross-sectional slices. Bottom left to right: 3D rendering of the entire mouse aorta, histogram of the 3D tomography data to elucidate differences in the real part of the refractive index.

Unfortunately, it was impossible to differentiate between the expected plaque and the arterial wall tissue. The histogram in Figure 2 only exhibits a shoulder of the main peak that might be caused from plaque formed. The hole easily recognized in the artery wall resulted from a bifurcation. Here, the vessel was trimmed off during specimen preparation.

The lumen of the mouse aorta has a cross-sectional area that ranges from 0.19 to 0.37 mm<sup>2</sup>. This means that the variation is below 50%. The 3D rendering illustrates that the lumen is rather straight and does not resemble the

morphology of a common stenosis in man. The periodic ripples along the vessel are artifacts that originate from insufficient background correction and can be removed by post-processing, which was not performed for the presented dataset.

### 3.3 Imaging an atherosclerotic human coronary artery

Three selected slices from the phase tomography and laboratory  $\mu$ CT were successfully registered in 2D space (Figures 3 and 4). This is a prerequisite to directly compare the performance of the two techniques. Registration was performed using a code developed by Kroon and Slump (multimodality non-rigid demon algorithm image registration [23]) in MATLAB 2010b with a scaling factor in the affine non-rigid registration. The two approaches provide similar information about the different tissue types and the paraffin embedding. Comparing the selected slices from the two approaches, however, the distinction is clearer in phase tomography than in the conventional  $\mu$ CT data. This qualitative observation is corroborated using the joint histograms represented between the slices. They are almost symmetric along the diagonal, a sign that both approaches are comparable in performance. One can clearly distinguish the paraffin (a), the soft tissues including muscles (b), and the plaque (c). The peaks of the components, however, have different half widths. For example, the paraffin peak is narrower for the phase tomography than for the advanced laboratory  $\mu$ CT, giving rise to an oval shape in the joint histogram (a).

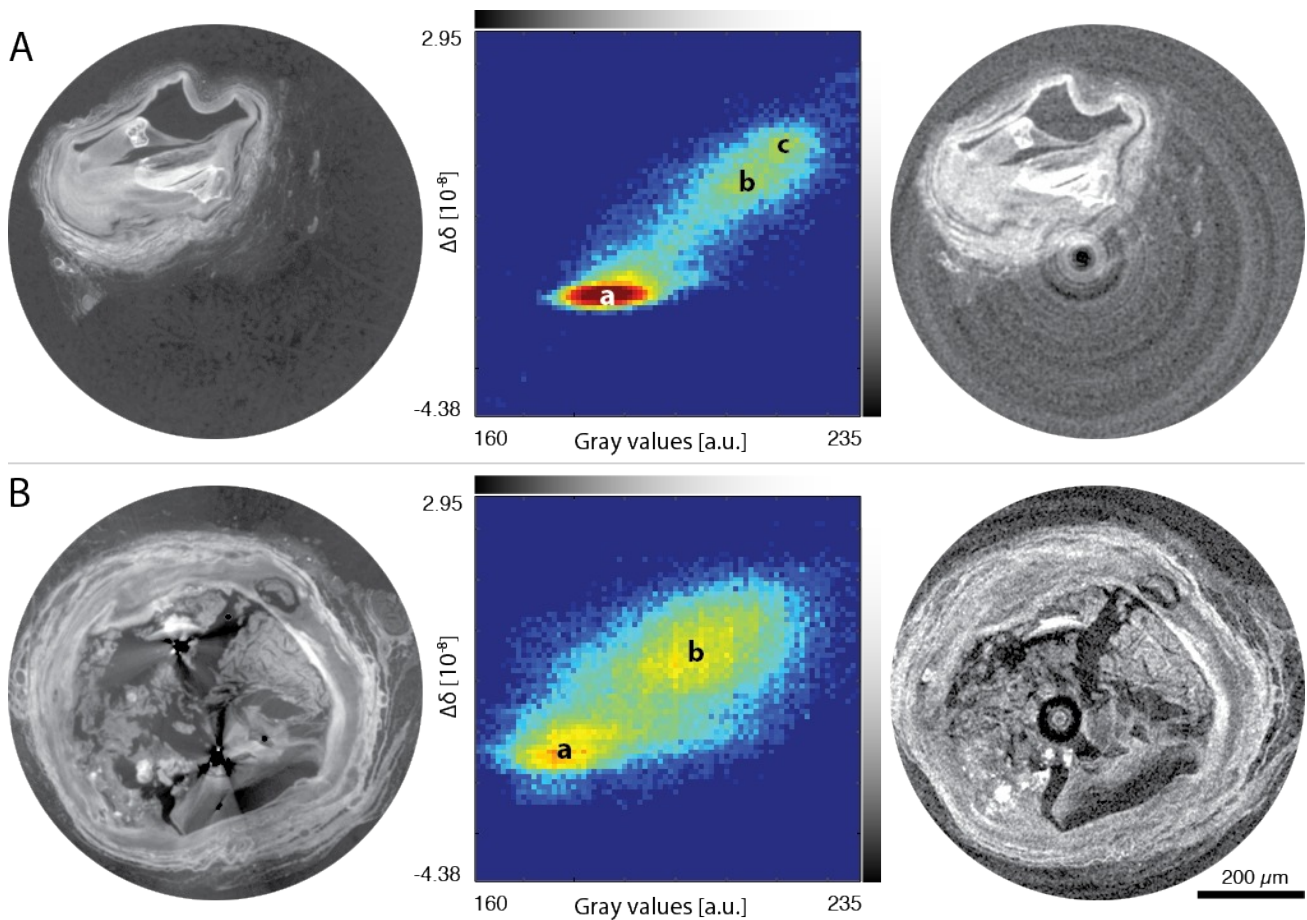


Figure 3. Comparison of phase tomography using synchrotron radiation and laboratory  $\mu$ CT for the extraction of lumen morphology. A and B show for two selected slices of the phase tomography (left), the joint histogram (center) and the laboratory  $\mu$ CT data (right). The joint histograms can be used to segment tissues by comparing the different gray-scale values in the slices, i.e. paraffin (indicated by a), muscle and soft tissues (b), and plaque (c).

The data does not allow an easy identification of different tissue types. Experts in anatomy can differentiate between the tissues because of their expertise and slightly preferred the quality of the phase tomography data. Here, they identified tissue structures such as smooth tissues, foamy cells, muscle walls and cholesterol. It has to be mentioned,

however, that the ring artifacts, which are much more prominent in the laboratory  $\mu$ CT data, create major peak broadening especially for the paraffin. The application of ring artifact corrections led to an inhomogeneous background in the laboratory  $\mu$ CT dataset not observed in the phase tomography data.

For flow simulations in the blood vessel system, the lumen of the stenosed vessels has to be determined. Although the phase tomography provides better contrast for tissue differentiation, the SR $\mu$ CT in the absorption contrast mode is much better suited for lumen segmentation. This surprising result is due to the nature of the artifacts present. In phase tomography, artifacts from the air bubbles led to such high differences in local  $\Delta\delta$ -values that the intensity-based segmentation by region-growing was impossible (cp. slice shown in Figure 4). The ring artifacts observed in laboratory  $\mu$ CT do not interfere with the segmentation procedure in the same manner. Therefore, the lumen from the data of the laboratory  $\mu$ CT was extracted from the 4.9 mm-long section of the artery (one slice given in Figure 4) using the region-growing tool of the software VG Studio Max 2.1 (Volume Graphics, Heidelberg, Germany). The cross-sectional area was analyzed using computer code (MATLAB R2010b). The artery showed a minimal cross-section of 0.83 mm<sup>2</sup> and a maximum cross-section of 5.60 mm<sup>2</sup>. This means the constriction corresponds to 85%.

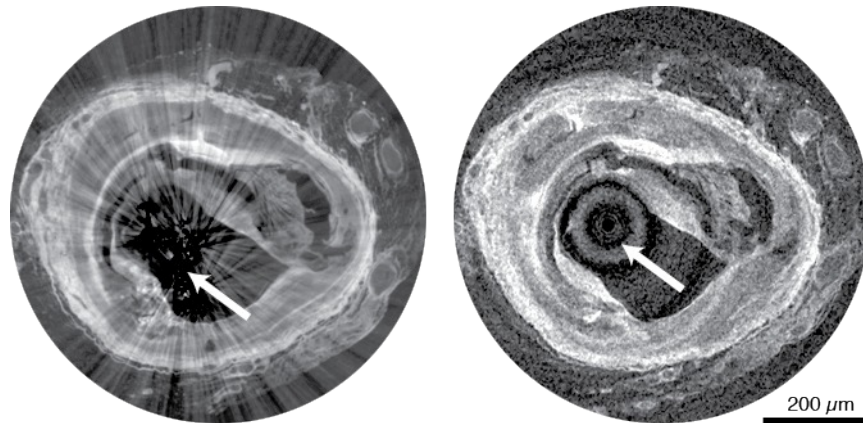


Figure 4. Comparison of phase tomography (left slice) and laboratory  $\mu$ CT (right slice) using a slice that contains an air bubble. The trapped air causes artifacts that prevent the segmentation of the vessel lumen in phase tomography data.

### 3.4 Multi-modal imaging of a slice of an atherosclerotic human coronary artery

The combination of modalities often yields additional information. Therefore, the combination of the tomography data with the histology might give additional insights into the tissue morphology. While tomography data contain X-ray absorption values and the real part of the refractive index for phase tomography, histology provides functional information depending on the stain applied. The disadvantage of histology, however, is the tremendous effort for serial sectioning and the limited spatial resolution in the third dimension, perpendicular to the slices. As a consequence researchers usually only prepare a limited number of histological slices. A 3D dataset of histological data is rarely generated.

An H&E-stained histological slice was prepared from the atherosclerotic human coronary artery after the decalcification and nondestructive  $\mu$ CT data acquisition. This slice was registered with the datasets from absorption-based SR $\mu$ CT and phase tomography in the manner described above. The three related slices are displayed in Figure 5: the phase SR $\mu$ CT data using red color, the absorption SR $\mu$ CT-data with green color, and the histology slice using the blue color. The superposition of the slices given in the bottom right of Figure 5 supplies an image that highlights the relative contributions.

The phase tomography slice, given in red, exhibits the biggest contrast between tissue types. The foamy cell region specified by the white circle in the RGB composite contains very low  $\Delta\delta$  values characterized using dark colors (almost black). In the phase SR $\mu$ CT slice, the relatively high  $\Delta\delta$  values characterized by bright red originate from plaque. An air bubble enclosed in the paraffin created the striking artifact, i.e. the pair of well-localized high brightness streaks highlighted by the white arrow.

Although the contrast between tissue types of the absorption SR $\mu$ CT-slice (green color) is lower than in phase tomography, one recognizes the artifacts from the residual plaque. This observation indicates that the decalcification

procedure was incomplete. Such an incomplete plaque extraction, however, can be an advantage, since the location of plaque is identified without strong streak artifacts.

The histological slice provides a higher spatial resolution than absorption SR $\mu$ CT and phase tomography slices. Thus, the details of the anatomical microstructures are more easily visible. The microstructures are similar in the three slices. There are, however, some noteworthy observations. The foamy cells and fat correspond to the green part of the RGB image, since these tissue types show up as black or very dark areas in the phase tomography and histology. The plaque is bright pink, as it is brightest in the phase tomography. The phase tomography and histology contribute mainly to the muscle and vessel walls, so they appear violet. The artifacts from the air bubble in phase tomography are prominent.

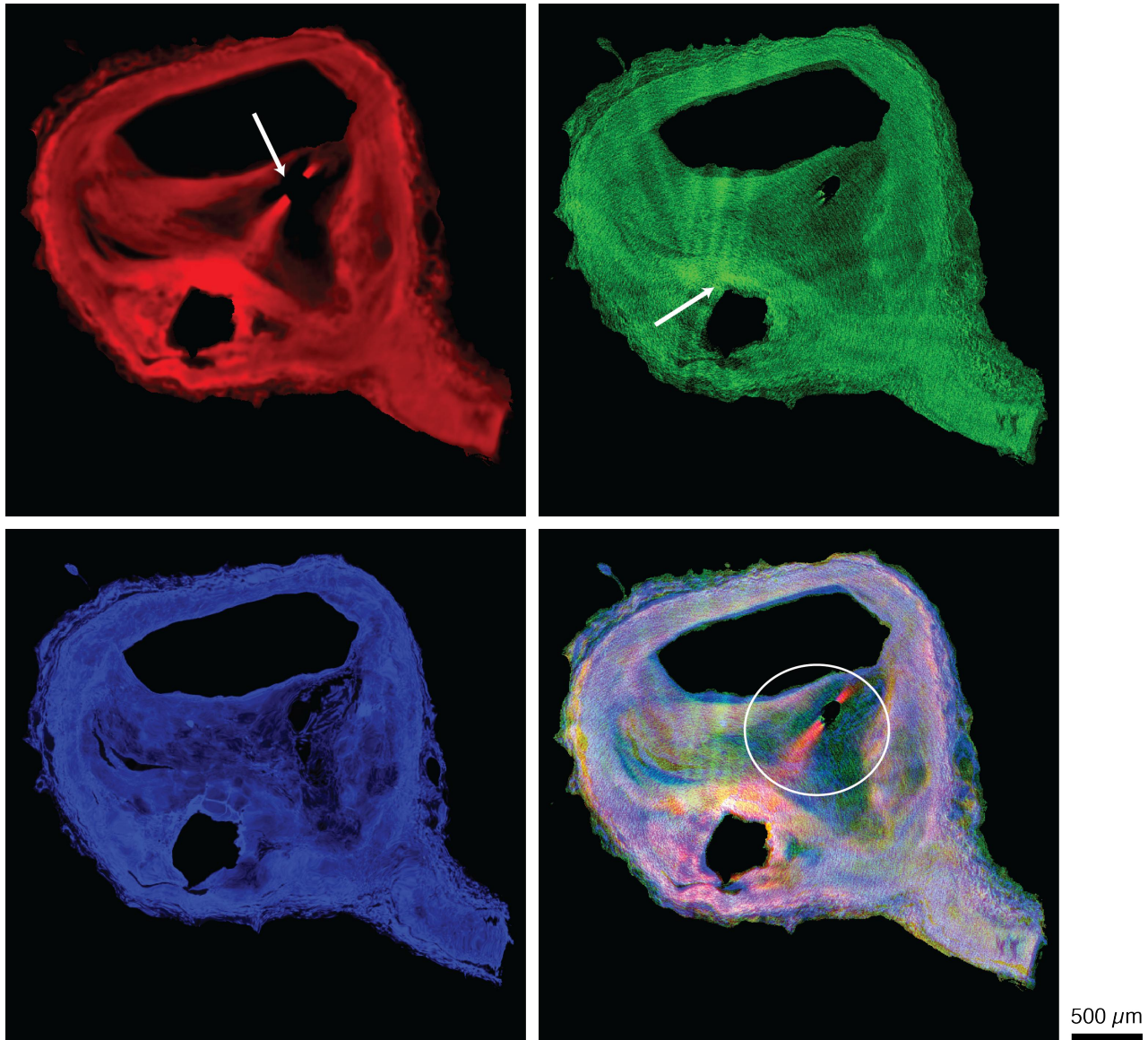


Figure 5: Comparison of phase tomography (red), absorption SR $\mu$ CT (green) and histology (blue) techniques for visualizing tissue types in a stenosed human coronary artery. Arrows indicate sources of artifacts: air bubble (phase tomography) and residual plaque (absorption SR $\mu$ CT). Bottom right: RGB composite image of the slices obtained from the three modalities. The white circle indicates the foamy cell region. The slice is situated just before a bifurcation. The protrusion in the bottom right of each image is the wall of the bifurcated artery. Dynamic range: The histogram of each image has been scaled to include only the tissue related peaks with values ranging from 0 to 255.

### 3.5 Arterial cross-section and extent of constriction

Table 1 lists the cross-sectional areas of the lumens derived from tomography data of the PMMA model, the mouse aorta and the human atherosclerotic artery. The constriction was calculated from the ratio of the cross-sectional areas, i.e. minimal cross-section divided by the maximal cross-section. Assuming a circularly shaped vessel, one finds the radius at the maximum stenosis, which is more common in literature.

Table 1. Morphological parameters of PMMA model, mouse, and atherosclerotic human vessels.

	Cross-section area [mm <sup>2</sup> ]				Maximum constriction [%]	Minimum radius [mm]
	Average	Maximum	Minimum	Std. dev.		
PMMA-model (healthy)	6.23	6.49	6.04	0.12	6.9	1.39
PMMA-model (diseased)	3.52	6.43	1.17	1.78	81.8	0.61
Mouse aorta	0.27	0.37	0.19	0.04	49.4	0.24
Human artery	2.31	5.60	0.83	1.36	85.2	0.51

## 4. DISCUSSION

### 4.1 Morphology of mouse artery

The mouse artery illustrated in Figure 2 show the challenge in the visualization of small specimens using grating-based phase tomography. During the grating interferometry experiment at the beamline W 2 the choice of the parameters was suboptimal. The third Talbot order, for example, leads to less sensitive images compared to the ninth Talbot order at the beamline ID 19. Due to beamtime restrictions, the experiment was carried out at a photon energy of 31 keV and not of 23 keV. The reduction of the energy leads to a higher sensitivity of the experimental setup. Despite these challenges, the phase tomography at the W 2 beamline was sufficient to segment the lumen of the mouse artery, which was the imaging task of the experiment. It was impossible to obtain the same image quality with conventional absorption-contrast tomography.

Although there is no constriction due to disease, the artery tapers to one end, giving rise to a maximum constriction of 49.4%. The average cross-sectional area of 0.27 mm<sup>2</sup> (Table 1) corresponds to a 96% occlusion of a human coronary artery of 2.5 mm diameter. Due to these favorable dimensions, the mouse aorta could potentially be of use in flow studies or *in vivo* experiments for, e. g. testing the localized release of a marker from shear-sensitive nanocontainers. However, unlike the PMMA-model and human arteries, the mouse aorta is a continuous tube with no sudden change in cross-sectional area. The investigated section has a standard deviation of only 0.04 mm<sup>2</sup>, approximately 2% that of the PMMA model and human arteries. Additionally, we were unable to identify any calcified plaques. It is possible that the animal's lifetime was insufficient to allow formation of calcified plaques, and that the disease model is not sufficiently representative of the pathology observed in human cases for these studies. This puts into question the usefulness of a mouse model for evaluating the role of shear stress in, e. g. targeted drug delivery in the human heart, cp. the recent paper of D. Ingber's team [24]. Vortex formation and re-flow phenomena have been observed in flow simulations where the morphology has a major role in determining local shear stresses. It must be validated whether the aorta can be successfully connected to a flow system, whether the lack of plaque and diseased tissue could lead to a difference in drug metabolism, and (with flow simulations) whether such a smooth morphology is an appropriate model.

### 4.2 Micro-morphology of atherosclerotic human coronary arteries

Registered slices of a human coronary artery measured by laboratory  $\mu$ CT and phase tomography (Figures 3 and 4) were examined for their usefulness a) as modalities for identifying different tissues types, and b) for segmenting the non-constricted cross-sectional area. The methods provide complementary results and the nature of the artifacts determined the limits of each dataset.

Laboratory  $\mu$ CT showed ring artifacts, which did not interfere with the segmentation tool (VG Studio Max 2.1, Heidelberg, Germany) used to extract the non-constricted cross-sectional area. This imaging modality is a fast, convenient method for extracting data about the lumen morphology (Table 1). However, the artifacts from the highly

absorbing plaque obscured the morphology of the calcified regions and led to a broadening of the histogram compared to phase tomography (Figure 3). Coupled with the larger pixel size of 17.78  $\mu\text{m}$ , it was impossible to identify all microstructures and therefore different tissue types. In contrast, phase tomography showed starburst artifacts caused by air bubbles in the paraffin formed during the embedding process (see Figures 4 and 5, phase tomography image, white arrow). This made segmentation of the lumen cross-sectional area impossible, but experts could identify different tissue types (foamy cells, calcifications, muscle etc.) and unstable plaques in phase tomography data by comparison with histology (Figure 5).

To see whether identification of different tissue types could be achieved in absorption-based tomography, absorption SR $\mu$ CT was also used as an imaging modality (Figure 5). Unfortunately, artifacts caused by the highly absorbing residual plaque (Figure 5, absorption SR $\mu$ CT image, white arrow) also made it impossible for the experts to reliably identify different soft tissue types.

Defining a critical stenosis is non trivial. The constriction is often defined in terms of reduction in diameter or cross-sectional area [25-28], but can also be considered in terms of fractional or coronary flow reserve [29]. Accuracy of detection methods also influences results. For example, synchrotron radiation coronary angiography is able to detect diameters of down to 100  $\mu\text{m}$  in beating hearts versus 400  $\mu\text{m}$  in conventional angiography [25]. Reports of 99% stenosis by diameter in the literature are common [25], although often stenoses are only qualitatively characterized as 'severe'. Nielsen and co-workers define stenosis as >70% constriction and healthy as <30% constriction [30], whereas DeMaria et al. define significant stenosis as >50% [31]. However, such basic criteria may be misleading, since the hemodynamic effect also depends on the lesion length, blood viscosity and laminar flow characteristics that dictate flow velocity and wall shear stresses [32]. Other studies consider  $\geq 75\%$  stenoses by diameter as critical [33]. ST-elevation myocardial infarction (STEMI) occurs when a culprit lesion completely blocks a vessel. Therefore, 81.8% constriction by diameter as seen in this study is a reasonable model for targeting the culprit lesion whilst avoiding most other, non-critical, stenoses.

### 4.3 PMMA-model to reproduce the morphology of healthy and atherosclerotic human coronary arteries

We were able to show that the PMMA-model presented similar morphology to a stenosed human coronary artery and was within a reasonable range according to the literature, and, therefore, appropriate to use in shear-release experiments as reported previously [4]. The maximum diameter of the healthy and diseased PMMA-model arteries is identical within error bars. The average diameter of the healthy artery PMMA model is 2.82 mm, within the values reported *in vivo* (normally 2 to 3 mm). The diseased artery PMMA-model exhibits a maximum occlusion of 81.8% cross-sectional area, corresponding to a minimum radius of 0.61 mm (Table 1). This is in accordance with constrictions reported in the latter stages of atherosclerosis based on measurements using, for example, angiography [34]. A critically stenosed artery (>80% stenosis) is of interest for studying release of a drug from a shear-stress sensitive nanocontainer [4]. The diseased model artery is within 1.8% of this value. Therefore, it is a reasonable approximation of a stenosed artery for further studies.

The human artery and diseased PMMA-model have similar properties, with the human artery possessing an 85.2% maximum constriction by cross sectional area versus 81.8% in the diseased PMMA model. This corresponds to a minimum radius of 0.51 and 0.61 mm respectively. The human artery has generally 10% smaller dimensions, with a maximum cross-sectional area of 5.60 mm<sup>2</sup> versus 6.27 mm<sup>2</sup> for the PMMA models. However, it shows slightly less range in occlusion, illustrated by a smaller standard deviation in cross-sectional area (1.36 mm<sup>2</sup> versus 1.78 mm<sup>2</sup> in the diseased PMMA model).

The PMMA model has a morphology that shows similar characteristics to the *in vivo* situation and is therefore very helpful for identification of nanocontainer formulations suitable for clinical studies, maybe even without any animal testing.

## 5. CONCLUSIONS

The PMMA model cross-sectional areas correspond well to the literature values in the case of both the healthy and diseased artery, with the latter falling in the severely stenosed category. Such a model is highly desirable for testing the suitability of shear stress sensitive nanocontainers as drug delivery vectors.

The mouse aorta, although it is not stenosed to 80%, does present the cross-sectional area corresponding to a 96% constriction of a 2.5 mm diameter human coronary artery. This is slightly higher than desired for testing the suitability of

shear stress sensitive nanocontainers. Although the constriction is a model for a critically stenosed artery, such as in, e. g. ST-segment elevation MI (STEMI), its usefulness as a morphological model is limited, since it has a smooth morphology.

Phase tomography gives high contrast images from which different tissues types can be identified by comparison with histology. However, artifacts from air bubbles make segmentation of the lumen unfeasible. This might be overcome by using PFA as a storage medium in place of paraffin. It is a useful tool for identifying the 3D morphology of tissue composition in decalcified human coronary arteries, when compared to histology as a reference. Laboratory  $\mu$ CT and absorption SR $\mu$ CT do not provide as much resolution of different tissue types, but are more appropriate for the extraction of the artery lumen. Artifacts in phase tomography from air bubbles introduced in the paraffin embedding are more problematic in the segmentation procedure than the ring artifacts caused by residual plaque in laboratory  $\mu$ CT and absorption SR $\mu$ CT. The various analysis tools provide a complementary analysis of tissue structure and morphology. A decalcified human coronary artery was found to present the desired morphology for testing the suitability of shear stress sensitive nanocontainers as drug delivery vectors.

## ACKNOWLEDGEMENTS

The project was mainly funded by the Swiss National Science Foundation in the National Research Program 62 "Smart Materials" framework and by the Swiss National Science Foundation grants to F. Mach (#310030-118245) and F. Montecucco (#32003B-134963/1). It was supported with beamtime from the ESRF (MD-498 and MI-983) and the HASYLAB at DESY (I-20100181 EC). The authors wish to thank K. Püschel of the Institute of Forensic Medicine, University Medical Center, Hamburg-Eppendorf for providing the human arteries. One of the authors (T. W.) received support from the French research networks (RTRA) 'Digiteo' and 'Triangle de la Physique' (grants 2009-034T and 2009-79D). The authors also thank C. David, who fabricated the gratings at the Paul Scherrer Institut, Villigen, Switzerland.

## REFERENCES

- [1] [Fact sheet N°317, [www.who.int](http://www.who.int)] World Health Organisation, (September 2011).
- [2] V. Fuster, P. R. Moreno, Z. A. Fayad *et al.*, "Atherothrombosis and high-risk plaque: Part I: Evolving concepts," *J. Am. Coll. Cardiol.*, 46(6), 937-954 (2005).
- [3] C. Cheng, F. Helderman, D. Tempel *et al.*, "Large variations in absolute wall shear stress levels within one species and between species," *Atherosclerosis*, 195(2), 225-235 (2007).
- [4] M. N. Holme, I. A. Fedotenko, D. Abegg *et al.*, "Shear-stress sensitive lenticular vesicles for targeted drug delivery," *Nature Nanotech.*, 7(8), 536-543 (2012).
- [5] U. Bonse, and F. Busch, "X-ray computed microtomography ( $\mu$ CT) using synchrotron radiation (SR)," *Prog. Biophys. Mol. Biol.*, 65(1), 133-169 (1996).
- [6] J. Herzen, F. Beckmann, T. Donath *et al.*, "X-ray grating interferometer for imaging at a second-generation synchrotron radiation source," *Proc. SPIE*, 7804, 780407 (2010).
- [7] T. Weitkamp, A. Diaz, C. David *et al.*, "X-ray phase imaging with a grating interferometer," *Opt. Express*, 13(16), 6296-6304 (2005).
- [8] V. Braunersreuther, A. Zerneck, C. Arnaud *et al.*, "Ccr5 but not Ccr1 deficiency reduces development of diet-induced atherosclerosis in mice," *Arterioscler. Thromb. Vasc. Biol.*, 27(2), 373-379 (2007).
- [9] J. Herzen, T. Donath, F. Beckmann *et al.*, "X-ray grating interferometer for materials-science imaging at a low-coherent wiggler source," *Rev. Sci. Instrum.*, 82(11), 113711 (2011).
- [10] S. H. Irsen, B. Leukers, C. Tille *et al.*, "Image based analysis of bone graft samples made by 3D printing using conventional and synchrotron-radiation-based micro-computed tomography," *Adv. Med. Eng.*, 114, 121-126 (2007).
- [11] B. Müller, G. Schulz, J. Herzen *et al.*, "Morphology of urethral tissues," *Proc. SPIE*, 7804, 78040D (2010).
- [12] F. Beckmann, J. Herzen, A. Haibel *et al.*, "High density resolution in synchrotron-radiation-based attenuation-contrast microtomography," *Proc. SPIE*, 7078, 70781D (2008).

- [13] A. Lareida, F. Beckmann, A. Schrott-Fischer *et al.*, "High-resolution X-ray tomography of the human inner ear: synchrotron radiation-based study of nerve fibre bundles, membranes and ganglion cells," *J. Microsc.*, 234(1), 95-102 (2009).
- [14] P. Thurner, F. Beckmann, and B. Müller, "An optimization procedure for spatial and density resolution in hard X-ray micro-computed tomography," *Nucl. Instrum. Methods Phys. Res. Sect. B*, 225(4), 599-603 (2004).
- [15] T. Weitkamp, C. David, C. Kottler *et al.*, "Tomography with grating interferometers at low-brilliance sources," *Proc. SPIE*, 6318, 63180S (2006).
- [16] T. Weitkamp, I. Zenette, C. David *et al.*, "Recent developments in X-ray Talbot interferometry at ESRF-ID19," *Proc. SPIE*, 7804, 780406 (2010).
- [17] G. W. Faris, and R. L. Byer, "Three-dimensional beam-deflection optical tomography of a supersonic jet," *Appl. Opt.*, 27(24), 5202-5212 (1988).
- [18] F. Pfeiffer, O. Bunk, C. David *et al.*, "High-resolution brain tumor visualization using three-dimensional x-ray phase contrast tomography," *Phys. Med. Biol.*, 52, 6923-6930 (2007).
- [19] F. Pfeiffer, O. Bunk, C. Kottler *et al.*, "Tomographic reconstruction of three-dimensional objects from hard X-ray differential phase contrast projection images," *Nucl. Instrum. Methods Phys. Res. Sect. A*, 580(2), 925-928 (2007).
- [20] S. Preibisch, S. Saalfeld, and P. Tomancak, "Globally optimal stitching of tiled 3D microscopic image acquisitions," *Bioinformatics*, 25(11), 1463-1465 (2009).
- [21] T. Walter, D. W. Shattuck, R. Baldock *et al.*, "Visualization of image data from cells to organisms," *Nat. Methods*, 7(6), 479-479 (2010).
- [22] B. Müller, F. Beckmann, M. Huser *et al.*, "Non-destructive three-dimensional evaluation of a polymer sponge by micro-tomography using synchrotron radiation," *Biomol. Eng.*, 19(2), 73-78 (2002).
- [23] D.-J. Kroon, and C. H. Slump, "MRI modality transformation in demon registration," *IEEE*, 963-966 (2009).
- [24] N. Korin, M. Kanapathipillai, B. D. Matthews *et al.*, "Shear-Activated Nanotherapeutics for Drug Targeting to Obstructed Blood Vessels," *Science*, 337(6095), 738-742 (2012).
- [25] S. Matsushita, K. Hyodo, T. Imazuru *et al.*, "The minimum coronary artery diameter in which coronary spasm can be identified by synchrotron radiation coronary angiography," *Eur. J. Radiol.*, 68(3, Supplement), S84-S88 (2008).
- [26] T. Hozumi, K. Yoshida, T. Akasaka *et al.*, "Noninvasive assessment of coronary flow velocity and coronary flow velocity reserve in the left anterior descending coronary artery by Doppler echocardiography: Comparison with invasive technique," *J. Am. Coll. Cardiol.*, 32(5), 1251-1259 (1998).
- [27] D. Hackett, J. Verwilghen, G. Davies *et al.*, "Coronary stenoses before and after acute myocardial infarction," *Am. J. Cardiol.*, 63(20), 1517-1518 (1989).
- [28] C. M. Gibson, L. Diaz, K. Kandarpa *et al.*, "Relation of vessel wall shear stress to atherosclerosis progression in human coronary arteries," *Arterioscler. Thromb. Vasc. Biol.*, 13(2), 310-315 (1993).
- [29] E. Shalman, M. Rosenfeld, E. Dgany *et al.*, "Numerical modeling of the flow in stenosed coronary artery. The relationship between main hemodynamic parameters," *Comp. Biol. Medicine*, 32(5), 329-344 (2002).
- [30] M. Böttcher, M. M. Madsen, F. Randsbæk *et al.*, "Effect of oral nitroglycerin and cold stress on myocardial perfusion in areas subtended by stenosed and nonstenosed coronary arteries," *Am. J. Cardiol.*, 89(9), 1019-1024 (2002).
- [31] M. Yamagishi, S. E. Nissen, D. C. Booth *et al.*, "Coronary reactivity to nitroglycerin: Intravascular ultrasound evidence for the importance of plaque distribution," *J. Am. Coll. Cardiol.*, 25(1), 224-230 (1995).
- [32] E. O. Ofili, M. J. Kern, A. J. Labovitz *et al.*, "Analysis of coronary blood flow velocity dynamics in angiographically normal and stenosed arteries before and after endolumen enlargement by angioplasty," *J. Am. Coll. Cardiol.*, 21(2), 308-316 (1993).
- [33] C. Bertolotti, and V. Deplano, "Three-dimensional numerical simulations of flow through a stenosed coronary bypass," *J. Biomech.*, 33(8), 1011-1022 (2000).
- [34] F. Ledru, P. Thérout, J. Lespérance *et al.*, "Geometric features of coronary artery lesions favoring acute occlusion and myocardial infarction: a quantitative angiographic study," *J. Am. Coll. Cardiol.*, 33(5), 1353-1361 (1999).